Ionisation of atoms by intense laser pulses

Tóth Attila
Department of Physics
Babeş-Bolyai University Cluj-Napoca

PhD Thesis Summary

Scientific Advisor: Prof. Dr. Nagy Ladislau

2013

Keywords

high intensity, ultrashort laser pulses, over-the-barrier ionisation, *ab-initio* solution of the time dependent Schrödinger equation, finite element discrete variable representation, Lanczos propagator, hydrogen atom, noble gases, temporal interference, spatial interference, light induced electron diffraction, holographic mapping

List of publications

- ISI articles

  1. S. Borbély, A. Tóth, K. Tőkési, and L. Nagy, *Spatial and temporal interference during the ionization of H by few-cycle XUV laser pulses*, Phys. Rev. A **87** (2013) 013405
  2. S. Borbély, A. Tóth, K. Tőkési, and L. Nagy, *Laser-induced electron diffraction in a pump-probe setup using half-cycle electric pulses*, Phys. Scr. **2013** (2013) 014066

- Articles in preparation

  1. S. Borbély, A. Tóth, K. Tőkési, and L. Nagy, *Ionization of atoms by few-cycle EUV laser pulses: carrier-envelope phase dependence of the intra-pulse interference effects*, Cent. Eur. J. Phys.
  2. S. Borbély, A. Tóth, K. Tőkési, and L. Nagy, *nemesgazos cikk*, Phys. Rev. A

Contents of the Thesis

Introduction

Over the last few decades, since their first experimental realisation in 1960 [1], lasers became integrated in our daily life. Due to the coherency and high monocromaticity of the light produced by lasers, they are used in a wide array of applications. These applications are ranging from industrial and commercial uses, such as material processing (cutting, welding, drilling, engraving), storing and retrieving data from optical discs, barcode readers, laser printers, optical communications just to mention a few, to military applications. Another area where laser technology is becoming increasingly important is medicine.

Beside the implementation of the various applications, laser technology continuously progressed. The achievable intensities became ever higher and in parallel pulsed lasers appeared with shorter and shorter pulse durations. A milestone in this development is the invention of the "chirped pulse amplification" (CPA) in 1985, which managed to overcome the technical limitations of previous lasers designs, bringing an increase of about six orders of magnitude for the achievable intensities. Accordingly, state of the art laser facilities are capable of producing ultra-short laser pulses with durations of the order of 10 fs, and intensities well above $10^{15}\mathrm{W/cm^2}$. These conditions opened the door for the investigation of new, previously unknown phenomena.

The dominant response of matter towards irradiation by an intense external field is ionisation, which can occur via multi-photon ionisation (MPI), tunnelling ionisation (TI) or over the barrier ionisation (OBI). The fundamental difference of field induced ionisation compared to impact ionisation with a charged particle is that the ejected electrons move under the influence of the oscillating external radiation field. Accordingly, these photoelectrons will have a quiver motion, and there is a good chance that they return sufficiently close to their parent ions in order to interact with them. These interactions can take various forms such as excitation or further ionisation, but there are two scenarios which lead to particularly interesting applications. In the first case, the returning electron recombines with the ion and consequently looses its excess energy by the emission of a single, high-frequency photon. This process is known as high harmonic generation (HHG). In the second scenario, instead of

being reabsorbed, the redirected electron is scattered on the residual ion. This way, the electron wave packet produced by the laser field can be used to obtain information regarding the structure of the target atom or molecule. This process is known as light-induced electron diffraction (LIED)[2, 3, 4, 5, 6]. In case of the LIED, under certain circumstances it is possible that beside the signal (diffracted) wave packet a reference (unscattered) wave is also present. The interference of these two wave packets leads to a radial fringe pattern in the momentum distribution of the free electrons [7, 8, 9], which can be interpreted as the holographic mapping (HM) of the target's state.

The timescale of almost all phenomena occurring in the quantum world is in the femtosecond regime or below. In order to investigate these fast processes a high temporal resolution of the detection technique is demanded. This suitable time resolution became available with the development of ultrashort laser pulses achieving pulse durations of a couple of fs or even below. This way, it is possible to follow the movement of atoms in molecules during chemical reactions [10], or the dynamics of bound electrons in atoms and molecules [11, 12].

The subject of the present thesis is the investigation of atomic systems irradiated by intense two-cycle EUV laser pulses. Due to the characteristics of the employed laser light, the corresponding field strength is comparable to the Coulombic bond between the electron and the nuclei, and a number of non-perturbative phenomena can take place. This makes perturbation theory inappropriate for the correct description of the systems dynamics, which leaves the direct solution of the time-dependent Schrödinger equation the only reliable approach.

Interaction of matter with external radiation fields

The second and third chapter of the present thesis are intended to serve as a short introduction into the world of laser-matter interaction. The discussion begins with a description of the fundamental concepts that lead to laser operation. Than, the various techniques, such as Q-switching, mode-locking, high harmonic generation, and chirped pulse amplification, that are essential to generate ultrashort and high intensity radiation are briefly described.

Next, a mathematical description of the laser fields is given. The notion of *gauge transformation* is introduced, than the validity of the classical description of the laser fields, and of the *dipole approximation* employed in our calculations is justified. Afterwards, the Hamiltonian formalism, necessary for the quantum mechanical description of the interaction of a charged particle with a radiation field is derived.

As the subject of the present thesis is the theoretical investigation of the ionisation of atoms, the various mechanisms through which ionisation can occur are presented. Depending on the parameters of the laser field, these are single-photon ionisation, multi-photon and above threshold ionisation, tunnelling and over-the-barrier ionisation.

In order to study the above presented ionisation processes, one has to solve the time dependent Schrödinger equation. An analytical solution of this problem does not exist, therefore two alternatives emerge. The obvious one is based on a direct numerical solution. The advantage of these methods is that they provide *exact* results, although at the expense of high computational resource demands. The second alternative is to consider some kind of justifiable approximations. This limits the applicability of the resulting method and reduces the accuracy of the results, but on the upside requires much less numerical computations. The most frequently used such approximate methods (perturbation theory, essential state model, Floquet model, Keldysh-Reiss-Faisal model, Coulomb-Volkov model and Ammosov-Delano-Krainov model) are presented briefly, concentrating mainly on their advantages and limitations. Than the attention is turned to the *ab-initio* approach employed in the present work.

Numerical solution of the time dependent Schrödinger equation

The time dependent Schrödinger (TDSE) equation is a partial differential equation which contains the first order derivative in time and up to second order spatial derivatives. In coordinate space, for a system of n-particles, it can be written as

$$i\frac{\partial}{\partial t}\Psi(\mathbf{r},t) = \hat{\mathbf{H}}(t)\Psi(\mathbf{r},t), \tag{1}$$

where $\mathbf{r}$ denotes the n-particle position vector. A numerical solution of equations of this type have two key aspects, namely the numerical representation of the $\Psi(\mathbf{r},t)$ functions at a given time moment (*spatial discretisation*) and the *propagation* of these functions until the desired final time moment. In the literature there are numerous methods to accomplish both of these goals, but here only those implemented in our numerical code will be presented. The number n of particles considered in the calculations increases drastically the computational requirements of the problem, meaning that current day computational resources are capable of treating exactly systems that consist of at most two electrons, i.e. the helium atom. For this reason, in our investigations we restrict ourselves to the interaction of a single electron with external radiation. This approach is exact for the description of the hydrogen atom. For the other, more complex atoms (noble gases) considered in our investigations, we employ the single active electron approximation (SAE), where only the outermost electron interacts with the laser field, while the others are included in the calculations as a simple static shielding of the nucleus.

Spatial discretisation

The wave functions associated to quantum systems span an infinite dimensional vector space of square integrable functions called the Hilbert space. In a numerical solution of the TDSE, due to the finite amount of

memory available in computers, the exact wave function has to be represented by a finite set of discrete values. Accordingly, in the calculations the continuous functions $\Psi(\mathbf{r},t)$ are replaced by vectors of finite length (N), while linear operators, such as the Hamiltonian or its constituents, are represented by square $(N \times N)$ matrices.

Even when only a single active electron is considered, the solution of the TDSE is a three dimensional (spatial) problem which is computationally demanding. However, considering the symmetry properties of the system, the calculations at hand can be simplified.

Time depending close-coupling

Due to the spherical symmetry of the binding potentials considered in our calculations, it is advantageous to recast the TDSE in spherical polar coordinates $(\{r,\theta,\phi\})$. Accordingly, the wave function can be expanded in the basis of spherical harmonics

$$\Psi(\mathbf{r},t) = \sum_{l=0}^{\infty} \sum_{m=-l}^{l} \frac{R_{l,m}(r,t)}{r} Y_l^m(\theta,\phi), \tag{2}$$

which is the core idea of the widely used time dependent close-coupling (TDCC) [13, 14] approach. Inserting this partial wave expansion into (1), and taking the inner product of both sides with $Y_l^{m^*}(\theta,\phi)$ gives

$$\begin{aligned} i\frac{\partial}{\partial t} \sum_{l=0}^{\infty} \sum_{m=-l}^{l} \frac{R_{l,m}(r,t)}{r} \int Y_{l'}^{m'^*}(\theta,\phi) Y_l^m(\theta,\phi) \mathrm{d}\Omega = \\ = \sum_{l=0}^{\infty} \sum_{m=-l}^{l} \left(\int Y_{l'}^{m'^*}(\theta,\phi) \hat{\mathbf{H}}(t) Y_l^m(\theta,\phi) \mathrm{d}\Omega \right) \frac{R_{l,m}(r,t)}{r}, \end{aligned} \tag{3}$$

where $d\Omega = \sin\theta d\theta d\phi$. This way the three-dimensional Schrödinger equation is reduced to an infinite set of coupled one-dimensional partial differential equations, which is much easier to handle than the original problem. Of course, in practical calculations the infinite set is truncated at a certain l_{max} value for which convergence is reached.

The $\left\langle Y_{l'}^{m'} \middle| \hat{\mathbf{H}}(t) \middle| Y_l^m \right\rangle$ matrix elements of the Hamiltonian can be eval-

uated analytically, leading to the close-coupling equation

$$i\frac{\partial}{\partial t}R_{l,m}(r,t) = \left[\frac{l(l+1)}{2r^2} - \frac{1}{2}\frac{\partial^2}{\partial r^2} - \frac{1}{r}\right] R_{l,m}(r,t) - \\ - qE(t)r\left[\sqrt{\frac{(l-m+1)(l+m+1)}{(2l+1)(2l+3)}}R_{l-1,m}(r,t) + \right. \\ \left. + \sqrt{\frac{(l-m)(l+m)}{(2l-1)(2l+1)}}R_{l+1,m}(r,t)\right] \tag{4}$$

in the length gauge description of the laser-electron interaction, and

$$i\frac{\partial}{\partial t}R_{l,m}(r,t) = \left[\frac{l(l+1)}{2r^2} - \frac{1}{2}\frac{\partial^2}{\partial r^2} - \frac{1}{r}\right] R_{l,m}(r,t) + \\ + i\frac{q}{m}A_z(t)\left[\sqrt{\frac{(l-m)(l+m)}{(2l-1)(2l+1)}}\left(\frac{\partial}{\partial r} - \frac{l}{r}\right)R_{l-1,m}(r,t) - \right. \\ \left. - \sqrt{\frac{(l-m+1)(l+m+1)}{(2l+1)(2l+3)}}\left(\frac{\partial}{\partial r} + \frac{l+1}{r}\right)R_{l+1,m}(r,t)\right]. \tag{5}$$

in the velocity gauge formalism.

Discretisation of the radial wave function

In order to solve the above presented close-coupling equations, the $R_{l,m}(r,t)$ radial wave functions still need to be discretised. For this purpose we employed the *finite element discrete variable representation* (FEDVR) [15, 16, 17, 18]. This is based on the finite element (FE) method, which implies the division of the configuration space into finite elements. In our 1D problem this means that the coordinate space is divided into segments with variable lengths, delimited by a set of nodes

$$r_{min} = r^1 < r^2 < \ldots < r^N = r_{max}. \tag{6}$$

In contrast with the spectral representation, the wave function is not expanded in terms of *global* functions, but it is represented by a set of *local* discrete variable representation (DVR) basis functions $f_m^{(i)}(r)$ defined only inside a given finite element ($f_m^{(i)}(r) = 0\ \forall m$ if $r \notin [r^{(i)}, r^{(i+1)}]$), which

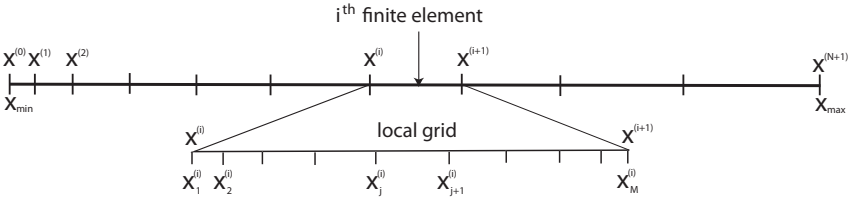

Figure 1: FE grid

define a local grid (see figure 1). The continuity of the wave function is ensured by placing the starting and ending point of the neighbouring local subgrids such a way that they overlap, which implies the use of a Gauss-Lobbato integration quadrature rule. Finally, the wave functions can be written as

$$\Psi(r) = \sum_{i=1}^{N} \sum_{j=1}^{M_i} w_j^{(i)} \Psi(r_j^{(i)}) f_j^{(i)}(r). \tag{7}$$

This approach brings together the advantages of both the FE and the DVR methods. That is, the flexibility provided by the FE method can be exploited to accurately represent the Coulomb singularity at the nucleus, by choosing sufficiently small finite elements in the vicinity of the core (it implies a denser grid). This has another advantage. Since most of the important dynamics, i. e. population transfer between bound states and bound-free transitions, takes place in that region, it is important to have a good resolution for the wave function. In contrast, free states (which span regions far from the nucleus) can reasonably well be described with fewer gridpoints, i.e. larger finite elements. The advantage of the DVR method is that similarly to the usual spectral representation techniques, it provides high accuracy for the calculation of derivatives. Moreover, in the FEDVR method, due to the local nature of the basis functions, the kinetic energy matrix elements $D_{mn} = \left\langle f_m^{(i)}(r) \left| \frac{\partial^2}{\partial r^2} \right| f_n^{(j)}(r) \right\rangle$ are different from zero only if the two basis functions involved are defined in the same finite element ($i = j$). Consequently, the kinetic energy matrix is composed of several small blocks which overlap at only one point. Also, with a good approximation, the potential energy operator's matrix representation is diagonal. This sparse structure of the Hamiltonian's matrix representation can be exploited to reduce the computational cost of the solution of the TDSE.

Time propagation

The solution of differential equations of type (1) is known in mathematics as an *initial value problem*. This means that at some arbitrary (initial) time moment t_0 the wave function $\Psi(\mathbf{r}, t \equiv t_0)$ is known, therefore the solution of the equation is equivalent with the determination of the time evolution of this initial state. The wave function at an arbitrary time moment can be expressed with the help of the so called *evolution operator*

$$\Psi(\mathbf{r}, t) = \hat{\mathbf{U}}(t, t_0)\Psi(\mathbf{r}, t_0). \tag{8}$$

This evolution operator can be expressed as

$$\hat{\mathbf{U}}(t + \Delta t, t) = \mathcal{T} \exp\left(-i \int_t^{t+\Delta t} \hat{\mathbf{H}}(t')\mathrm{d}t'\right), \tag{9}$$

where $\mathcal{T}$ denotes the time-ordering operator, which must be present due to the non-commutivity of the Hamiltonian at different time moments $\left(\left[\hat{\mathbf{H}}(t_1), \hat{\mathbf{H}}(t_2)\right] \neq 0\right)$. The direct evaluation of the above equation is inconvenient, therefore in all practical cases the time interval over which the TDSE needs to be solved is divided into subintervals over which the Hamiltonian does not change appreciably. Consequently, the evolution operator corresponding to the individual subintervals reduces to

$$\hat{\mathbf{U}}(t + \Delta t, t) \simeq \exp\left(-i\hat{\mathbf{H}}(t)\Delta t\right). \tag{10}$$

With this result the TDSE can be solved by successive application of the appropriate evolution operators on the initial wave function

$$\begin{aligned}\Psi(\mathbf{r}, t_0{+}n\Delta t) = \exp\left[-i\hat{\mathbf{H}}(t_0 + (n-1)\Delta t)\Delta t\right] \times \ldots \\ \times \exp\left[-i\hat{\mathbf{H}}(t_0 + \Delta t)\Delta t\right] \exp\left[-i\hat{\mathbf{H}}(t_0)\Delta t\right] \Psi(\mathbf{r}, t_0).\end{aligned} \tag{11}$$

In order to evaluate the right hand side of equation (11), one has to know how to apply the exponential of an operator on a wave function. Such an exponential can be expanded in Taylor series as

$$\exp\left(-i\hat{\mathbf{H}}(t)\Delta t\right) = \sum_{n=0}^{\infty} \frac{1}{n!} \left(-i\hat{\mathbf{H}}(t)\Delta t\right)^n, \tag{12}$$

therefore the action of the exponential on the wave function can be easily evaluated since the power of an operator is nothing else than

$$\left(-i\hat{\mathbf{H}}(t)\Delta t\right)^n \Psi(\mathbf{r},t) = \underbrace{\left(-i\hat{\mathbf{H}}(t)\Delta t\right) \times \ldots \times \left(-i\hat{\mathbf{H}}(t)\Delta t\right)}_{n \ \ times} \Psi(\mathbf{r},t). \tag{13}$$

This propagation scheme is known as the *Taylor propagator*.

There is another, more direct way to evaluate the right hand side of equation (11). This is done by the explicit evaluation of the $\exp\left(-i\hat{\mathbf{H}}(t)\Delta t\right)$ matrix exponential, which leads to the

$$\exp\left(-i\hat{\mathbf{H}}(t)\Delta t\right)\Psi(\mathbf{r},t) = \left[\mathbf{\Phi}^{-1} diag\left(e^{-iE_1\Delta t}, e^{-iE_2\Delta t}, \ldots\right)\mathbf{\Phi}\right]\Psi(\mathbf{r},t) \tag{14}$$

propagation scheme, where $\mathbf{\Phi}$ represents a column matrix built from the Φ_k eigenvectors of the instantaneous Hamiltonian operator, while $diag\left(e^{-iE_1\Delta t}, e^{-iE_2\Delta t}, \ldots\right)$ is the diagonal matrix of the exponential of its eigenenergies.

Employing this approach is too demanding from a computational point of view, since it requires the diagonalisation of a large matrix at each timestep. For this reason we implemented the *Lanczos* method, which is the state-of-the-art approach used by leading groups working on the theoretical investigation of laser-matter interaction. The first step of the method is to generate the Krylov subspace K_{n+1} of order $n+1$ by repeated action of the Hamiltonian on the initial state $\mid \Psi_0 \rangle = \Psi(\mathbf{r},t)$ as

$$\begin{aligned} K_{n+1} &= \left\{|\Psi_0\rangle, \hat{\mathbf{H}}|\Psi_0\rangle, \hat{\mathbf{H}}^2|\Psi_0\rangle, \ldots, \hat{\mathbf{H}}^n|\Psi_0\rangle\right\} \\ &= \left\{|\Psi_0\rangle, |\Psi_1\rangle, |\Psi_2\rangle, \ldots, |\Psi_n\rangle\right\}. \end{aligned} \tag{15}$$

Afterwards, the Gram-Schmidth procedure is used to obtain an orthonormal set of vectors that span K_{n+1}

$$Q_{n+1} = \left\{|q_0\rangle, |q_1\rangle, |q_2\rangle, \ldots, |q_n\rangle\right\}. \tag{16}$$

Now, it is possible to transform the Hamiltonian into an $(n+1)\times(n+1)$ matrix $\hat{\mathbf{h}}$ in the Q_{n+1} basis

$$\hat{\mathbf{H}} \simeq \hat{\mathbf{H}}^Q = \mathbf{Q}\hat{\mathbf{h}}\mathbf{Q}^\dagger, \tag{17}$$

where $\mathbf{Q}$ is a column matrix made from the q_k vectors. Accordingly, the evolution operator can be approximated as

$$\begin{aligned}\hat{\mathbf{U}}(t+\Delta t,t) \simeq \hat{\mathbf{U}}^{Q}(t+\Delta t,t) &= \exp\left(-i\hat{\mathbf{H}}^{Q}\Delta t\right) = \mathbf{Q}\exp\left(-i\hat{\mathbf{h}}\Delta t\right)\mathbf{Q}^{\dagger} \\ &= \mathbf{Q}\left[\mathbf{\Phi}^{\dagger} diag\left(e^{-i\epsilon_1\Delta t},\ldots,e^{-i\epsilon_{n+1}\Delta t}\right)\mathbf{\Phi}\right]\mathbf{Q}^{\dagger}.\end{aligned} \tag{18}$$

This last equality shows that the Lanczos algorithm is appealing because $-i\hat{\mathbf{h}}\Delta t$ can be inexpensively exponentiated according to equation (14), since $n \ll N$, where N is the dimension of the discretised Hamiltonian. The time stepping can be simplified using the associativity property of matrix-matrix multiplications

$$\begin{aligned}\Psi(\mathbf{r},t+\Delta t) &= \hat{\mathbf{U}}^{Q}(t+\Delta t,t)\Psi(\mathbf{r},t) \\ &= \mathbf{Q}\left\{\mathbf{\Phi}^{\dagger} diag\left(e^{-i\epsilon_1\Delta t},\ldots,e^{-i\epsilon_{n+1}\Delta t}\right)\left[\mathbf{\Phi}\left[\mathbf{Q}^{\dagger}q_0\right]\right]\right\},\end{aligned} \tag{19}$$

and due to the orthonormality of the q vectors this equation can be reduced to

$$\begin{aligned}\Psi(\mathbf{r},t+\Delta t) &= \mathbf{Q}\left[\mathbf{\Phi}^{\dagger} diag\left(e^{-i\epsilon_1\Delta t},\ldots,e^{-i\epsilon_{n+1}\Delta t}\right)\Phi_1\right] \\ &= \sum_{k=0}^{n} a_k|q_k\rangle,\end{aligned} \tag{20}$$

where Φ_k is the k^{th} column of the $\mathbf{\Phi}$ matrix formed from the eigenvectors of $\hat{\mathbf{h}}$, and the expansion coefficients are given by

$$\begin{aligned}a_k &= \Phi_{k+1}\, diag\left(e^{-i\epsilon_1\Delta t},\ldots,e^{-i\epsilon_{n+1}\Delta t}\right)\Phi_1 \\ &= \sum_{j=1}^{n+1}\Phi_{k+1}(j)e^{-i\epsilon_j\Delta t}\Phi_1(j).\end{aligned} \tag{21}$$

Calculation of observable quantities

The most complete information that can be acquired from an ionisation process is the fully differential momentum distribution of the ejected electron. We calculate this quantity by projecting the wave function onto the

$\psi_{\mathbf{k}}(\mathbf{r})$ continuum functions, which leads to

$$\frac{dP}{d\mathbf{k}} = |\langle \psi_{\mathbf{k}}(\mathbf{r}) \mid \Psi(\mathbf{r},t)\rangle|^2 = \left| \sum_{l=0}^{\infty} \sum_{m=-l}^{l} \frac{1}{k} i^{-l} e^{i\sigma_l} Y_l^m(\hat{\mathbf{k}}) \int_0^{\infty} \phi_{k,l}(r) R_{l,m}(r,t) dr \right|^2 . \quad (22)$$

For a purely Coulombic potential (ionisation of the hydrogen atom) these continuum functions can be obtained analytically (regular Coulomb functions). In case of our calculations employing the single active electron approximation (SAE) for the description of more complex systems, the continuum functions are obtained by the numerical solution of the appropriate time independent Schrödinger equation with the Numerov method. The obtained fully differential momentum distribution is used to calculate other relevant quantities such as the photoelectron spectrum (integrating over $\hat{\mathbf{k}}$), the angular distribution of the ejected electrons (integrating over $|\mathbf{k}|$) and the total ionisation probability (integrating over $\mathbf{k}$).

Before starting to use the newly built numerical code, its reliability had to be tested. For this reason we performed extensive convergence test, i.e. studied how the change of the numerical parameters affects the quality of the output. These parameters are mainly determined by the parameters of the considered laser pulse, and are the following: the size of the simulation box, the density of the numerical grid, and the size of the timestep used in the propagation. We found that for appropriately chosen parameters, our results are only limited by machine precision. In order to further validate our implementation, we compared our results with that obtained from an independently written code [19]. As it can be seen on figure 2 an excellent agreement was obtained.

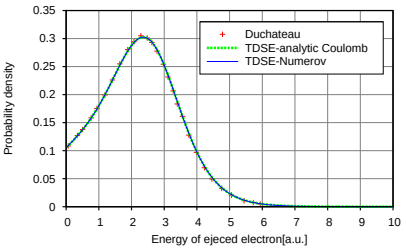

Figure 2: Energy spectrum of the ejected electrons: + calculations performed by Duchateau *et. al*; TDSE-analytic Coulomb − spectrum obtained by projecting the wave function onto analytically obtained Coulomb functions; TDSE-Numerov − spectrum obtained by projecting the wave function onto numerically obtained continuum functions.

Ionisation of atoms by few-cycle laser pulses

The aim of the present work is to investigate the various structures that appear in the fully differential momentum distribution of the photoelectrons, and to determine their origin. In order to achieve this, we employ ultra-short, two-cycle laser pulses described by

$$\mathbf{E}(t) = \begin{cases} \hat{\boldsymbol{\epsilon}} E_0 \sin^2\left(\frac{\pi t}{\tau}\right) \sin(\omega t + \varphi_0), & 0 \le t \le \tau \\ 0, & \text{otherwise} \end{cases} , \tag{23}$$

which is a plane wave modulated by a a sine-square envelope function. We set the carrier-envelope phase to be

$$\varphi_0 = -\frac{\omega\tau}{2} - \frac{\pi}{2} \tag{24}$$

in order to describe a time symmetric laser pulse (the maximum of the carrier wave coincides with the maximum of the envelope function). The temporal profile of the electric component of such a pulse is presented on figure 3. We used linearly polarised laser pulses along the z direction, and we set the carrier frequency to be $\omega = 0.4445$ a.u., which corresponds to a wavelength of $\lambda = 102$ nm (Ultraviolet range), and the strength of the field to $E_0 = 1$ a.u., which corresponds to an intensity of $I = 3.51 \times 10^{16}\mathrm{W/cm^2}$. During the numerical solution of the TDSE (time propagation) we have access at all times to the time dependent wave function. In order to identify the processes that occur during the interaction of the target atom with the laser field, we used these wave functions to calculate various physical quantities. In figure 4 snapshots on the time evolution of the momentum

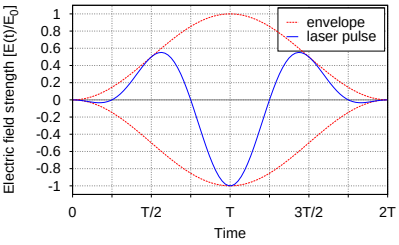

Figure 3: Temporal profile of the two-cycle laser pulse used in our calculations, where $T = 2\pi/\omega$ is the period of the carrier wave.

distribution of the free electrons is presented as a function of momentum components parallel (k_{par}) and perpendicular (k_{per}) to the laser polarisation. Above each momentum distribution, the laser pulse is plotted with a verical line indicating the time moment when the snapshot was taken.

At the beginning of the laser pulse ($t < 5$ a.u.), the continuum electrons show a dipole-like momentum distribution (see figure 4a)) indicating single-photon ionisation. Taking a look at figure 5, where the total ionisation probability is plotted as a function of time, we can conclude that the overall contribution of this process is negligible. Progressing further in time, the strength of the laser field undergoes a fast increase,

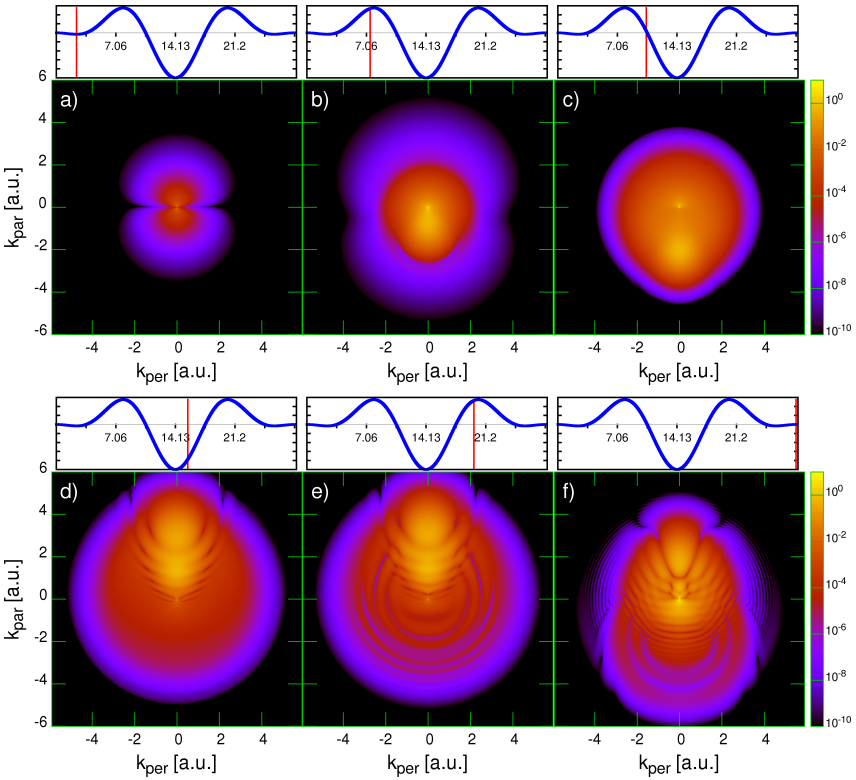

Figure 4: Momentum distribution of the continuum electrons as a function of parallel and perpendicular momentum components at different time moments indicated by the vertical lines on the laser pulse.

which results in a sudden increase of the total ionisation probability between $t \approx 5$ and 10 a.u.. The corresponding momentum distributions show that the photoelectrons are mainly emitted in the direction of the laser field polarisation, and they exhibit a strong forward-backward asymmetry (see figure 4 b)-c)). This indicates that the dominant ionisation process is tunnelling and over-the-barrier ionisation. We calculated the value of the critical field's strength at which OBI appears. The moment when the laser field reaches this value is indicated by vertical lines on the insets of figure 5, where, for a closer inspection, the total ionisation probability is plotted on a logarithmic scale. It can be seen, that the rapid ionisation of the target occurs in the time interval when the $E > E_{crit}$ condition is fulfilled, which consolidates that the undergoing ionisation process is OBI. The resulting electronic wave packet is moving under the combined action of the electric fields generated by the parent ion and the laser pulse. Initially, under the action of the laser field, it departs from the vicinity of the parent ion (figure 4 c)). Next, when the direction of the field changes, it is driven back to the core, and a characteristic radial pattern appears in the momentum distribution (figure 4 d)). This can be attributed to the scattering of the wave packet by the parent ion. Later on, concentric rings of maxima and minima appear in the ionisation probability density (see figure 4 e)). This pattern can be attributed to a temporal interference, i.e. coherent superposition of wave packets liberated from the atom at different time moments by the laser pulse. By now, all the dominant features are present in the momentum distribution. The remaining minor changes are due to the further quiver motion of the electrons and due to the electron recapture at the end ($t > 21$ a.u.) of the laser pulse (figure 4 f)).

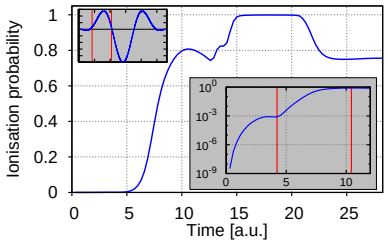

Figure 5: Total ionisation probability as a function of time. The inset present: the laser pulse (upper left); zoom of total ionisation probability on a logarithmic scale. On both insets the vertical red lines represent the time moments when the condition for OBI is fulfilled.

Temporal interference

As pointed out in the previous section, the concentric circles of maxima and minima in figure 4 e) may be explained as the result of the interference between the electronic wave packets emitted at different parts of the laser pulse, i.e. at different time moments. This process can be interpreted as a double- (multi-) slit interference in time domain [20], and it was studied in detail by several groups both theoretically [9, 21, 22, 23] and experimentally [20, 24]. A more detailed quantitative analysis of the process can be performed employing the strong field approximation (SFA). In this picture, the effect of the core's Coulomb potential on the free electrons is neglected. The first wave packet is emitted at time moment t_1 with momentum $\mathbf{k}_1(t_1)$, while the second at time t_2 with $\mathbf{k}_2(t_2)$, and they are added coherently in the continuum if the

$$\mathbf{k}_1(t_2) = \mathbf{k}_2(t_2) \tag{25}$$

condition is fulfilled. In the framework of the SFA the phase difference between the two wave packets can be calculated, and the temporal interference pattern is given by

$$I(\mathbf{k}, t_1, t_2) \sim \left| 1 + \mathrm{e}^{i\Delta\phi(\mathbf{k}, t_1, t_2)} \right| . \tag{26}$$

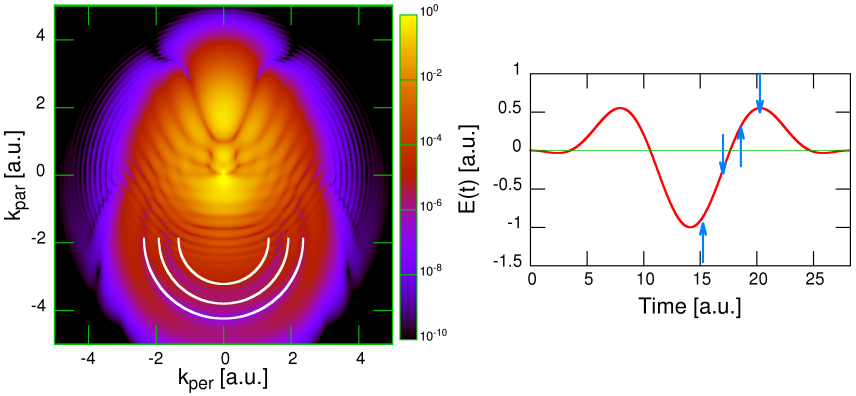

Figure 6: SFA interference rings (white circles) on top of the TDCC ionisation probability density expressed as a function of parallel and perpendicular momentum components. On the right figure, the "up arrows" indicate the $\{15.25, 18.59\}$, while the "down arrows" indicate the $\{17.00, 20.26\}$ pair of $\{t_1, t_2\}$ values.

By fitting the SFA interference pattern of equation (25) to the one obtained during the exact TDCC calculations (figure 4 e)), we were able to calculate the t_1 and t_2 emission times for the interfering electron wave packets. We have found two pairs of $\{t_1, t_2\}$ values (see figure 6 right part). In the left part of figure 6 one can observe the SFA extrema rings (indicated by white circles), which are in good agreement with the TDCC calculations.

Spatial interference

Now, let us turn our attention to the other, more prominent structure of the momentum distribution of the free electrons by first reviewing the undergoing processes. According to the three step model, when an atom or molecule is illuminated with a sufficiently intense laser radiation, free electronic wave packets are emitted via tunnelling or over-the-barrier ionisation. Under the action of the external field they are first accelerated away from the core, then, as the field changes its direction, they are turned back. The returning wave packets with low transverse momenta arrive in the near vicinity of the target ion and interact with it. This interaction can lead to different processes such as reabsorption or scattering of the wave packet. When recombination occurs, the excess energy of the electrons, gained from the field, is released in a burst of high-energy photons. This process is known as high harmonic generation.

Alternatively, the returning wave packet may scatter on the core. Since these laser-induced electronic waves are fully coherent, in the angle-resolved photoelectron spectra, this scattering manifests in the form of a diffraction pattern. Moreover, as the returning wave packet travels in the field of the parent ion, it encodes spatial information of this field, which can be retrieved from the resulting diffraction pattern. This self-imaging process is known as laser-induced electron diffraction (LIED) [2, 3, 4, 5].

Recent papers [7, 8, 9] have suggested that the radial fringe structure present in the momentum distribution of the free electrons originate from an alternative process to LIED. In this scenario, scattering on the parent ion still has a central role, but the crucial aspect is the difference of the final phases accumulated by electronic wave packets emitted during the same quarter-cycle of the driving laser pulse which follow different paths. In [7] it was pointed out, that under suitable conditions, only one of the above mentioned paths involves collision with the ion,

while the wave packet with larger transverse momenta which follows the other path is propagating without being affected by the core potential.

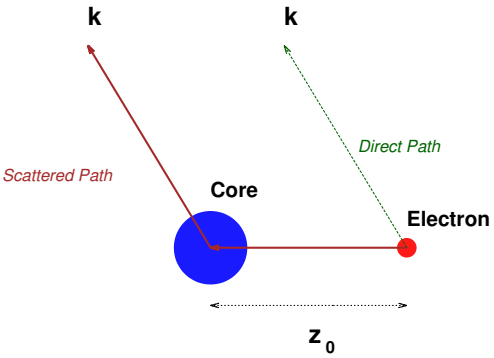

Figure 7: The direct and scattered electron trajectories in the two-path model.

Since the laser-induced free electronic waves are fully coherent, the concept of holography can be employed to interpret the interference structure in the momentum distribution as the holographic mapping (HM) of the target atom's or molecule's state. Since the position and shape of these interference extrema are strongly influenced by the short range potential describing the structure of the target, the HM is a potentially powerful tool to investigate the dynamic structure of atoms and molecules.

In their publication [7], Huismans *et. al* proposed a simple, intuitive model to grasp the essence of the HM. In their model electronic wave packets are formed via tunnelling ionisation at a z_0 distance from the core, and may follow either a direct or a scattered path, as represented schematically on figure 7. If the core is considered as an uniform point scatterer, the phase difference accumulated by the electrons associated with the two possible trajectories can be calculated analytically as

$$\Delta\phi = (k - k_z)z_0, \tag{27}$$

where k is the final momentum, k_z is the momentum component in the z direction, while z_0 is the distance to the point scatterer. With this expression, the spatial interference pattern can be given as

$$I(\mathbf{k}) \sim \left|1 + \mathrm{e}^{i(k-k_z)z_0}\right|. \tag{28}$$

Key to the HM is the existence of a distinct signal and reference wave, which is realised if the free electrons appear at a large z_0 distance from the core via tunnelling ionisation. As we have seen, in case of the laser parameters employed in our calculations the free wave packets are formed by OBI, which means that they appear in the immediate vicinity of the

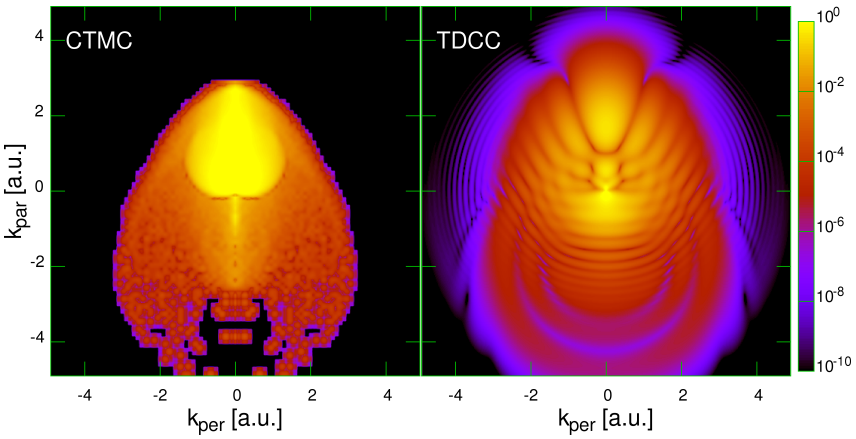

Figure 8: Ionisation probability densities as a function of parallel and perpendicular momentum components obtained in the framework of the CTMC and TDCC models.

core. However, under the action of the field they depart to a certain distance from the parent ion before they are redirected. Consequently, the two path model is applicable for our investigations.

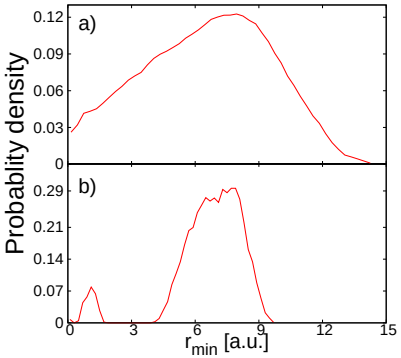

Figure 9: The distribution of r_{min} values for (a) all CTMC trajectories, and (b) CTMC trajectories with $0.5 < k_{per} < 0.7$ and $0.7 < k_{par} < 0.9$. The distributions were normalised to 1.

In order to test the validity of the basic assumptions of the model, i.e. the existence of the two distinct electron paths, our external collaborator Károly Tőkési performed classical stochastic calculations in the framework of the classical trajectory Monte Carlo (CTMC) method [25]. With the exception of the interference effects, which are of quantum origin, a good overall agreement can be observed between the TDCC and CTMC momentum distributions (see figure 8). The general agreement allowed us to perform detailed analysis of the CTMC electron trajectories. From the trajectories provided by the CTMC cal-

culation we selected those which contribute to the formation of the HM pattern, namely those where the electron is ionised at the very beginning of the laser pulse and then are redirected towards the parent ion by the laser field. For each of these trajectories, we have calculated the minimal distance r_{min} between the core and the electron in the return phase. If all selected trajectories are considered, the obtained distribution of r_{min} values is broad (see figure 9(a)), without any characteristic feature. However, if we consider only those CTMC trajectories where the asymptotic momentum is fixed (these are the ones that interfere with each other), the distribution completely changes. We will have two well separated groups of trajectories (see figure 9(b)): those with small r_{min} considered to be scattered, and those with large r_{min} considered to be direct. Hence, these findings confirm the assumption of the two-path model.

Influence of the laser pulse parameters

The main prediction of the two-path model is that the density of the HM interference fringes is determined by the value of z_0, i.e. how far the liberated electronic wave packet departs from the parent ion before recollision. According to equation 27, with increasing z_0 the HM interference pattern becomes denser. The value of z_0 depends mainly on the value of the average velocity of the of the electronic wave packet, and on how much time the wave packet has to depart from the parent ion before it is returned. By varying the parameters of the laser pulse we are able to control both the velocity and the return time of the wave packets, thus influence z_0 indirectly.

First, we have fixed the laser field frequency at $\omega = 0.4445$ a.u. and decreased the field strength gradually from $E_0 = 1$ a.u. down to $E_0 = 0.1$ a.u.. By doing so, we have decreased the average velocity of the wave packets, and implicitly z_0. Furthermore, we have fixed the velocity of the electronic wave packets by fixing the $\Delta k \sim E_0 T$ momentum transfer from a half-cycle of the laser field to the electron, and by increasing the period of the laser pulse we have increased the time interval available for the wave packet to propagate away from the core. This inherently increases the z_0 distance reached by the wave packet before its return. The behaviour of the HM pattern obtained for the various field parameters was in good qualitative agreement with the predictions of the two-path model, that is, by increasing the z_0 distance the density of the HM pattern also increases.

For the complete characterisation of ultra-short laser pulses contain-

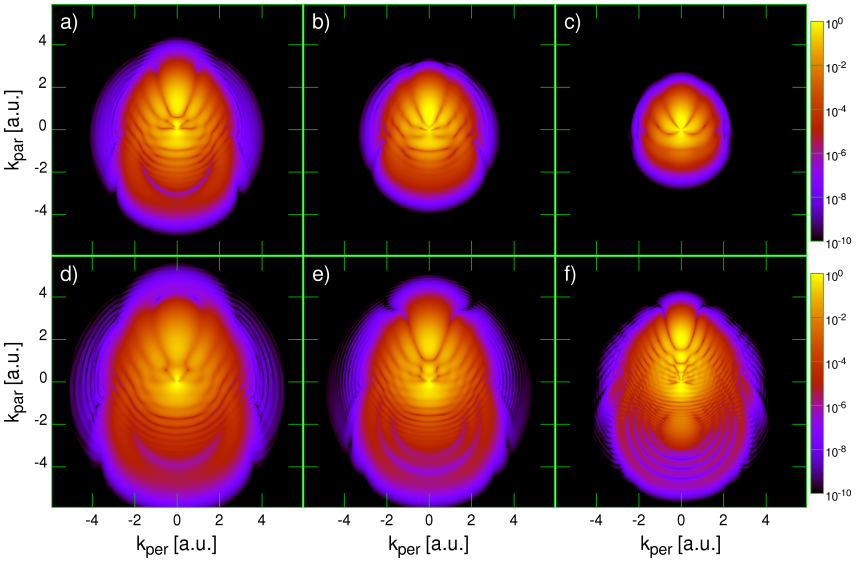

Figure 10: Ionisation probability densities as a function of parallel and perpendicular momentum components at different field parameters. Upper row: fixed ω =0.4445 a.u., $\tau = 28.27$ a.u.; (a) E_0=0.75 a.u.; (b) E_0=0.5 a.u.; (c) E_0=0.25 a.u.; Lower row: the momentum transfer to the electron over one half cycle is kept constant $\Delta k \simeq E_0 T/2 = 7.06$ a.u.; (d) $\omega = 0.66675$ a.u, $\tau = 18.84$ a.u., $E_0 = 1.5$ a.u.; (e) $\omega = 0.4445$ a.u, $\tau = 28.27$ a.u., $E_0 = 1$ a.u.; (f) $\omega = 0.22225$ a.u, $\tau = 56.51$ a.u., $E_0 = 0.5$ a.u..

ing only a few oscillations of the field, one also has to know the carrier-envelope phase (CEP). In order to investigate the dependence of the HM interference pattern on the CEP, we have performed calculations for the ionisation of the H atom by two-cycle laser pulses with carrier frequency $\omega = 0.4445$ a.u. for several CEP values $\varphi_0 \in \{0°, 30°, 60°, 90°, 120°, 150°\}$. The obtained momentum distributions of the continuum electrons for $E_0 = 1$ a.u are presented on figures 11. It can be observed that the shape of the field is highly sensitive to the CEP, and as a result, the entire dynamics of the system is changed when different CEP values are considered. We found that in order to obtain a clear HM interference pattern it is desirable that only one scattering to take place, which is the case for laser pulses with large asymmetry of the neighbouring pulse peak strengths predominantly in the $60° \leq \varphi_0 \leq 90°$ CEP region.

We continued to study the HM on the hydrogen atom by employing a simple pump-probe setup (see figure 12), which grasps the essence of

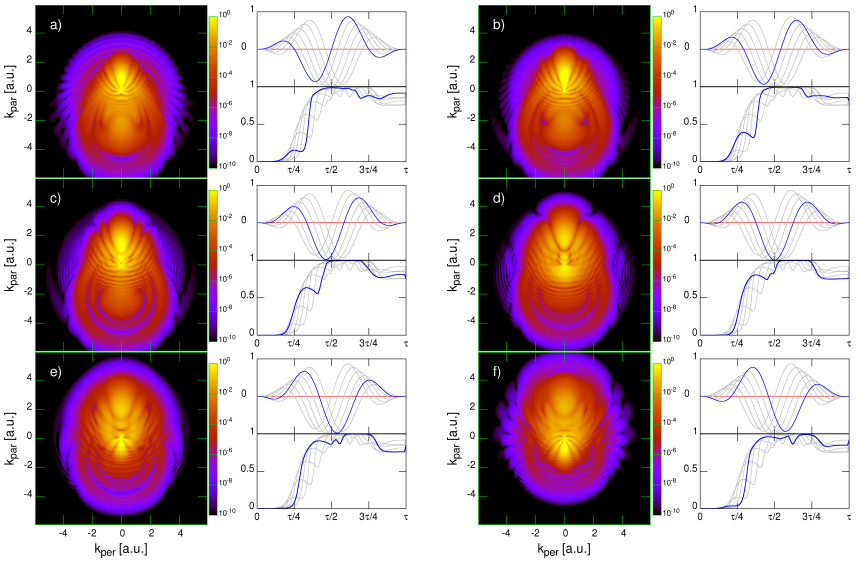

Figure 11: Momentum distribution of the continuum electrons as a function of parallel and perpendicular momentum components at the end of a two-cycle pulse with $\omega = 0.4445$ a.u. and $E_0 = 1$ a.u. for the following CEP values: a) $\varphi_0 = 0°$, b) $\varphi_0 = 30°$, c) $\varphi_0 = 60°$, d) $\varphi_0 = 90°$, e) $\varphi_0 = 120°$, f) $\varphi_0 = 150°$. On the right side of each momentum distribution the temporal profile of the corresponding field $E(t)/E_0$, and the total ionisation probability ($P(t)$) is plotted as a function of time.

the involved process. In this setup a continuum electronic wave packet is formed by the ionisation of the target with a half-cycle electric pulse (i.e. the pump pulse.). Using a second half-cycle pulse (i.e. the probe pulse), the previously formed wave packet is redirected toward the parent ion, where it scatters, leading to the formation of the characteristic interference pattern in the momentum distribution of the free electrons. The average distance z_0 reached by the free electronic wave packet, before it is turned back by the probe

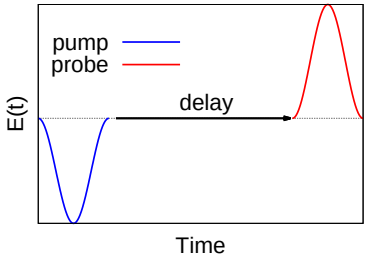

Figure 12: Shape of the electric pulses used in our pump-probe setup.

pulse, was directly controlled by the delay between the pump and the probe pulse. Larger delay meant that the electrons had more time to propagate away from the core, and consequently they reached a larger z_0 distance. We found that in accordance with our previous conclusions, and with the predictions of the two-path model, with the increase of z_0 the density of the HM interference extrema also increased. Next, we investigated the influence of the final average velocity v_z of the continuum electrons on the HM pattern. This parameter was controlled by the strength of the probe pulse. We concluded that v_z only influences the shape and position of the interference extrema, but it does not change their number.

Influence of the core potential - Ionisation of noble gases

The importance of the HM is that it provides spatial and temporal information about the investigated target. As the returning wave packet incident on the target travels in the potential of the residual ion, structural information of this ion is encoded in the scattered electrons wave function, with the obvious condition that they are sufficiently energetic (the corresponding de Broglie wavelengths have to be comparable to the length scales over which the shape of the investigate structures change). This means that the obtained HM pattern can be considered as a snapshot of the target taken at the moment of recollision. In real atoms and molecules, after the creation of a free wave packet, i.e. ejection of an electron from a bound state to the continuum, the residual electron cloud readjusts to the new configuration. For molecules this materialises in the variation of bond lengths. According to [6], temporal information about the evolution of the ion's structure can be obtained by "taking snapshots" at different time instants. This can be easily achieved by employing laser pulses with a number of different wavelengths.

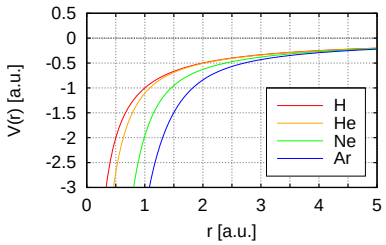

Figure 13: SAE model potentials of different noble gas atoms

In order to investigate the behaviour of the HM pattern toward changing the target atom, we performed calculations for different noble gases in the framework of the single active electron approximation.

In this picture only the outermost electron is treated explicitly, while the rest (if any) of them are only providing a static shielding of the nucleus. This way, the active electron is initially bound in a model atom described by a pseudo potential given by

$$V(r) = -\frac{Z_c + a_1 e^{-a_2 r} + a_3 r e^{-a_4 r} + a_5 e^{-a_6 r}}{r}, \tag{29}$$

where the parameters were optimised to provide ionisation potentials in good agreement with the experimentally obtained values. The resulting

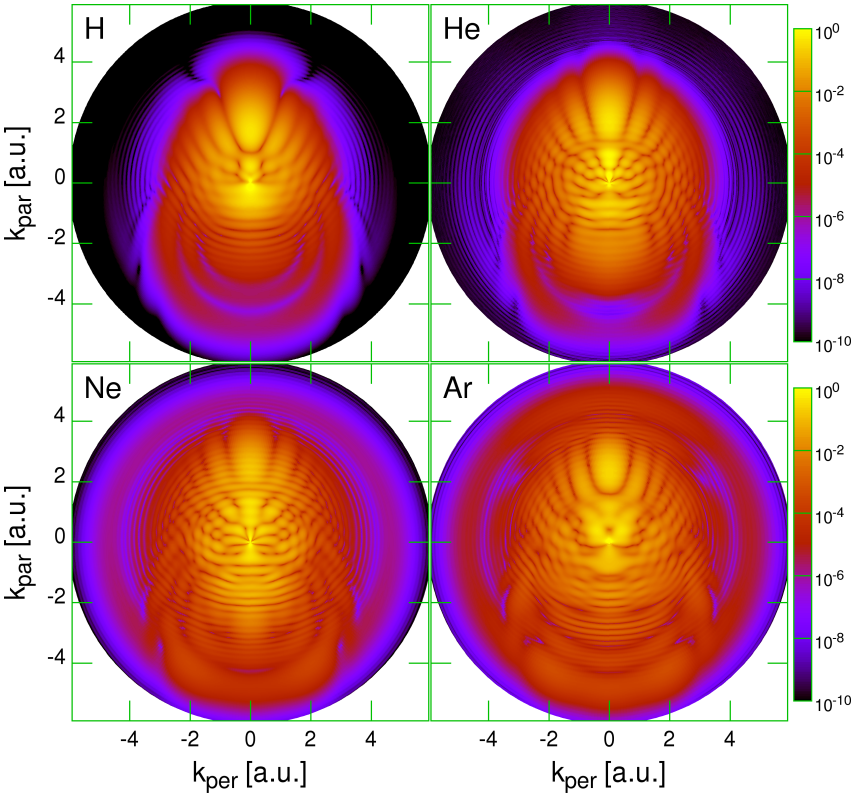

Figure 14: Momentum distribution of the continuum electrons as a function of parallel and perpendicular momentum components for different target atoms as indicated on the figures. Laser pulse parameters: $E_0 = 1.00$ a.u., $\omega = 0.4445$ a.u., $\varphi_0 = 90°$.

model potentials are plotted on figure 13, where it can be observed that they differ considerably only in the near vicinity of the core.

It is clear that in this SAE formalism the residual ions do not suffer any structural changes, the scattered electrons simply map the bare Coulomb potential in case of H, and the static SAE potentials for the other noble gases. In figure 14 the momentum distributions of the free electrons at the end of a laser pulse with $\omega_0 = 0.4445$ a.u, $\varphi_0 = 90°$ and $E_0 = 1$ a.u. are presented for the different target atoms. It can be observed that the potential experienced by them clearly has a large influence on the resulting HM patterns. Looking at figure 15, where the total ionisation probabilities and the expectation values of the z coordinate are plotted as a function of time for the considered target atoms, one can see that the Ar atom behaves similarly to the H while the behaviour of the He is similar to that of the Ne. The prominent difference between the two groups is the existence of a secondary interference structure in the low momentum region of the velocity maps. The precise examination of the wave packet dynamics leading to the formation of this secondary interference pattern will be the subject of further research. Nevertheless, what we can say is that under the action of the third peak of the laser pulse the low momentum components of the free wave packet, which did not depart too far from the core are driven back to its near vicinity. In case of the H and Ar atoms, this part of the free wave packet is recaptured (see the decrease in the total ionisation probability), while in case of He and Ne it is rescattered leading to the secondary HM pattern.

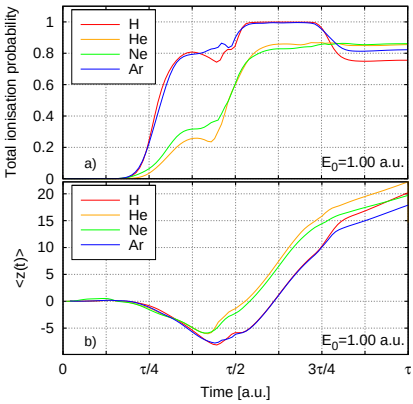

Figure 15: a) total ionisation probabilities as a function of time ; b) expectation value of the z coordinate as a function of time for the different noble gas targets.

As we have seen, the studied atoms can be divided in two groups according to the dynamics of the liberated electronic wave packets. Nevertheless, the momentum distributions obtained for the atoms in the same group are different: the HM pattern obtained for Ar and Ne is denser than the one obtained for H and He, respectively. This can be explained by

the following reasoning. When a free electron is moving toward its parent ion, it is accelerated by the potential of the ion. Analogously, after it is scattered and departs from the core, it is decelerated to its initial velocity. Now, looking at figure 13, we can see that the short range part of the Ar and Ne atom's potentials are "deeper" than that of the H and He, respectively. As a result the free electrons that scatter off the Ar (Ne) ion undergo a larger velocity change than the ones that move in the field of the N (He) atom. Consequently, they accumulate a greater phase difference compared to the reference electrons, which follow paths that do not involve collision with the target. This larger phase difference ultimately leads to a denser HM interference pattern.

Conclusions

In the present thesis we have investigated theoretically the interaction of atoms with ultrashort and intense linearly polarised laser pulses. To this end, we employed numerical methods for the direct solution of the time dependent Schrödinger equation. Most of the work was invested in the development of a new numerical code which is able to treat any problem that arises when a *single active electron* initially bound in a spherically symmetric static potential interacts with a linearly polarised laser field. This was achieved in the framework of the TDCC method by the discretisation of the TDSE on a FEDVR numerical grid and by propagation of the time dependent wave function of the active electron using the Lanczos algorithm.

After we have established that our numerical program is working correctly by performing various convergence checks, and comparing the produced results with theoretical data obtained by other groups, we started to investigate the interaction between the hydrogen atom and intense two-cycle EUV laser pulses. First, we identified the processes that occur during the action of the laser pulse. We found that most of the electrons are liberated by OBI, when the instantaneous intensity of the field increases above a critical value. After ionisation, secondary processes may occur, which leave their imprint on the final momentum distribution. We identified two such secondary process. The first one is a temporal interference between electronic wave packets emitted at different time moments, while the second one is a spatial interference between wave packets that are born in the same time instance but follow different paths. This spatial interference pattern can be considered as the holographic image of the target atom, meaning that beside the dynamics of the free electron, structural and temporal information about the target is also encoded in the momentum distribution. By performing TDCC calculations, we investigated the behaviour of the HM pattern as a function of the pulse parameters. We found that the dynamics of the free electronic wave packets is greatly influence by the CEP. The clearest HM pattern was observed when the free wave packet scatters strongly only once on the core, which is the case in the $60^\circ \leq \varphi_0 \leq 90^\circ$ CEP range. For this reason, in all our other calculations we used laser pulses characterised by $\varphi_0 = 90^\circ$.

By modifying consecutively the intensity of the field and the wavelength of the carrier wave, in agreement with the simple two-path model of [7], we concluded that the shape of the HM pattern is mainly determined by the z_0 parameter, which measures how far the free wave packet departs from the parent ion before it is driven back by the laser field. This result was also validated by a different set of calculations, where instead of the two-cycle laser field we employed two separate half-cycle electric pulses in a pump-probe setup, which allowed us to easily modify z_0 as well as the average velocity of the returning wave packet. Finally, in order to test the sensitivity of the HM pattern toward the potential experienced by the scattered electrons, which is the essential aspect of this technique as long as applications are concerned, we performed TDCC calculations for the He, Ne and Ar atoms in the framework of the SAE approximation. We found that the ionisation potential is an important factor in the determination of the undergoing processes. Accordingly, the studied atoms can be classified in two groups displaying similar dynamics, with the H and the Ar forming one, while the He and Ne the other. More importantly, the influence of the target atom's static potential on the HM pattern was confirmed.

Bibliography

[1] T. H. Maiman. *Nature* (1960) **187** 493. 1

[2] M. Okunishi, T. Morishita, G. Pruper, K. Shimada, *et al. Phys. Rev. Lett.* (2008) **100** 143001. 2, 16

[3] S. Micheau, Z. Chen, A. T. Le, J. Rauschenberger, *et al. Phys. Rev. Lett.* (2009) **102** 073001. 2, 16

[4] J. Xu, Z. Chen, A.-T. Le, and C. D. Lin. *Phys. Rev. A.* (2010) **82**. 2, 16

[5] C. D. Lin, A.-T. Le, Z. Chen, T. Morishita, *et al. J. Phys. B.: At. Mol. Opt. Phys.* (2010) **43**. 2, 16

[6] C. I. Blaga, J. Xu, A. D. DiChiara, E. Sistrunk, *et al. Nature* (2012) **483** 194–197. 2, 22

[7] Y. Huismans, A. Rouzée, A. Gijsbertsen, J. H. Jungmann, *et al. Science* (2011) **331** 61–64. 2, 16, 17, 27

[8] T. Marchenko, Y. Huismans, K. J. Schafer, and M. J. J. Vrakking. *Phys. Rev. A.* (2011) **84** 053427. 2, 16

[9] X.-B. Bian, Y. Huismans, O. Smirnova, K.-J. Yuan, *et al. Phys. Rev. A.* (2011) **84** 043420. 2, 15, 16

[10] A. H. Zewail. *J. Phys. Chem. A* (2000) **104 (24)** 5660–5694. 2

[11] M. Drescher, M. Hentschel, R. Kienberger, M. Uiberacker, *et al. Nature* (2002) **419** 803. 2

[12] M. Uiberacker. *Nature* (2007) **446** 627. 2

[13] M. S. Pindzola, F. Robicheaux, S. D. Loch, J. C. Berengut, *et al. J. Phys. B.: At. Mol. Opt. Phys.* (2007) **40** R39–R60. 5

[14] M. S. Pindzola and F. Robicheaux. *Phys. Rev. A.* (1998) **57**. 5

[15] T. N. Rescigno and C. W. McCurdy. *Phys. Rev. A.* (2000) **62** 032706. 6

[16] C. W. McCurdy, D. A. Horner, and T. N. Rescigno. *Phys. Rev. A.* (2001) **63** 022711. 6

[17] B. I. Schneider, L. A. Collins, and S. X. Hu. *Phys. Rev. E.* (2006) **73** 036708. 6

[18] B. I. Schneider, J. Feist, S. Nagele, R. Pazourek, *et al. Quantum Dynamic Imaging: Theoretical and Numerical Methods.* Springer (2011). 6

[19] G. Duchateau, E. Cormier, and R.Gayet. *Eur. Phys. J. D* (2000) **11** 191. 11

[20] F. Lindner, M. G. Schätzel, H. Walther, A. Baltuška, *et al. Phys. Rev. Lett.* (2005) **95** 040401. 15

[21] D. G. Arbó, E. Persson, and J. Burgdörfer. *Phys. Rev. A.* (2006) **74** 063407. 15

[22] D. G. Arbó, K. L. Ishikawa, K. Schiessl, E. Persson, *et al. Phys. Rev. A.* (2010) **82** 043426. 15

[23] D. G. Arbó, K. L. Ishikawa, K. Schiessl, E. Persson, *et al. Phys. Rev. A.* (2010) **81** 021403(R). 15

[24] R. Gopal, K. Simeonidis, R. Moshammer, T. Ergler, *et al. Phys. Rev. Lett.* (2009) **103** 053001. 15

[25] K. Tőkési and G. Hock. *Nucl. Instrum. Methods Phys. Res. Sec. B* (1994) **86** 201. 18